

Facile synthesis of pH-responsive gadolinium(III)-doped carbon nanodots with red fluorescence and magnetic resonance properties for dual-readout logic gate operations

Yaning Fang, Lefei Zhou, Junkai Zhao, Yali Zhang, Mo Yang, Changqing Yi

Abstract

The great challenge still exists in the synthesis of red-emissive carbon nanodots (C-dots) and the development of molecular logic devices with better operation stability for biological applications. In this study, gadolinium (III)-doped C-dots are synthesized by a new solvothermal approach using citric acid, urea and $GdCl_3$ as precursors. The as-prepared Gd^{3+} -doped C-dots exhibit bright red fluorescence (FL) centered at 620 nm in an excitation wavelength-independent manner, and a high T1 relaxivity ($\sim 16.0 \text{ mM}^{-1} \text{ s}^{-1}$). More excitingly, the Gd^{3+} -doped C-dots exhibit a pH-dependent response in not only FL behaviour but also magnetic resonance (MR) signal. When triggered by H^+ , OH^- , or Cu^{2+} , the Gd^{3+} -doped C-dots can behave as a switch for FL emission and MR signal, leading to dual-readout and multi-addressable logic systems. Therefore, by employing the Gd^{3+} -doped C-dots as logic gate with varying the chemical inputs, FL/MR dual-readout logic operations including IMP and NOR have been successfully demonstrated not only in all-aqueous media but also within the living HeLa cells. Together with the good biocompatibility and cell-permeability, the Gd^{3+} -doped C-dots hold great potentials for real-time monitoring pH changes both in solution and biological cells, and even future evaluating cellular states via in-cell biocomputation.

1. Introduction

Carbonic nanomaterials including carbon nanotubes, graphite nanoplatelets and carbon nanodots (C-dots), are considered to be the next generation of green nanomaterials.

Especially, C-dots have gained increasing research attentions in sensing, imaging, theranostics, electronic devices and etc [[\[1\]](#), [\[2\]](#), [\[3\]](#), [\[4\]](#), [\[5\]](#), [\[6\]](#), [\[7\]](#), [\[8\]](#)]. The obvious fascination is driven by their remarkable features such as facile synthesis and tunable surface functionalities, resistance to photobleaching, excellent biocompatibility and water solubility, and high photo/chemical stability. Although numerous interesting applications have been successfully demonstrated using C-dots, continuous efforts have been emphasized on improving their functionality and broadening their applications.

The increasing demands of information technology for miniaturization and function density prompts the research community to develop intelligent materials which can serve as molecular logic gates to conduct molecular computing and provide measurable output [[\[9\]](#), [\[10\]](#), [\[11\]](#), [\[12\]](#), [\[13\]](#), [\[14\]](#), [\[15\]](#)]. Enlightened by the pioneering work of de Silva in 1993 [[\[16\]](#)], all 16 fundamental logic gates, advanced circuits, and even neural network molecular logic gate, have been successfully demonstrated using various chemical systems including organic fluorophores, biomacromolecules and nanomaterials

[[\[16\]](#), [\[17\]](#), [\[18\]](#), [\[19\]](#), [\[20\]](#), [\[21\]](#), [\[22\]](#), [\[23\]](#), [\[24\]](#), [\[25\]](#), [\[26\]](#), [\[27\]](#), [\[28\]](#), [\[29\]](#), [\[30\]](#), [\[31\]](#), [\[32\]](#), [\[33\]](#), [\[34\]](#), [\[35\]](#), [\[36\]](#)]. Although the promising performance of the reported materials, it is still compelling to investigate new intelligent materials for advanced molecular logic gates which show better operation stability and applicability for biomedical applications.

Due to their remarkable features such as excellent biocompatibility and water solubility, high sensitivity and rapid response, C-dots are considered to be the key player in molecular computing. To perform molecular logic operations, photons and/or molecules usually act as chemical inputs, and the changes in luminescence, absorbance or electrochemical signals are monitored as measurable outputs. Meanwhile, C-dots have been engineered to sense various analytes, such as anions and metal ions, small molecules, as well as biomacromolecules. The fundamental mechanism of a C-dots-based sensor is the change in optical properties of C-dots upon their specific interactions with target analytes. Therefore, it is feasible to develop C-dots-based

molecular logic gates *via* chemically triggered fluorescence (FL) switch of C-dots. Actually, various C-dots-based molecular logic systems, such as AND, INHIBIT, NOR, NAND, OR, XOR, have been successfully demonstrated by utilizing various chemical stimuli [\[37\]](#), [\[38\]](#), [\[39\]](#), [\[40\]](#), [\[41\]](#), [\[42\]](#), [\[43\]](#). However, the development of C-dots-based logic gate with multi-readout which can significantly improve the operation stability, still pose significant challenges.

It has been well-established that element doping is a convenient strategy to tune the chemical composition and thereby physical properties of carbonic nanomaterials [\[44\]](#), [\[45\]](#), [\[46\]](#), [\[47\]](#), [\[48\]](#), [\[49\]](#), [\[50\]](#). In particular, doping magnetic elements such as Gd^{3+} or Ho^{3+} can render the resultant C-dots the capability of contrast enhancement in magnetic resonance (MR) imaging [\[46\]](#), [\[47\]](#), [\[48\]](#), [\[49\]](#), [\[50\]](#). Therefore, by engineering the Gd^{3+} -doped C-dots, the molecular events in logic systems is possibly transformed into both FL and MR changes, which in turn can be used as measurable outputs. In this study, the Gd^{3+} -doped C-dots which exhibit both the FL and MR response switch upon interaction with $H^+/OH^-/Cu^{2+}$ in aqueous solution, are synthesized and demonstrated for the development of a FL/MR dual-readout logic system in this study ([Fig. 1](#)). IMP and NOR logic operations have been successfully implemented in aqueous media by observing the change in both the FL and MR response with varying the chemical inputs. More excitingly, a living cell imaging-based IMP logic gate operation has also been successfully demonstrated, emphasizing the feasibility of C-dots-based molecular devices for biomedical research.

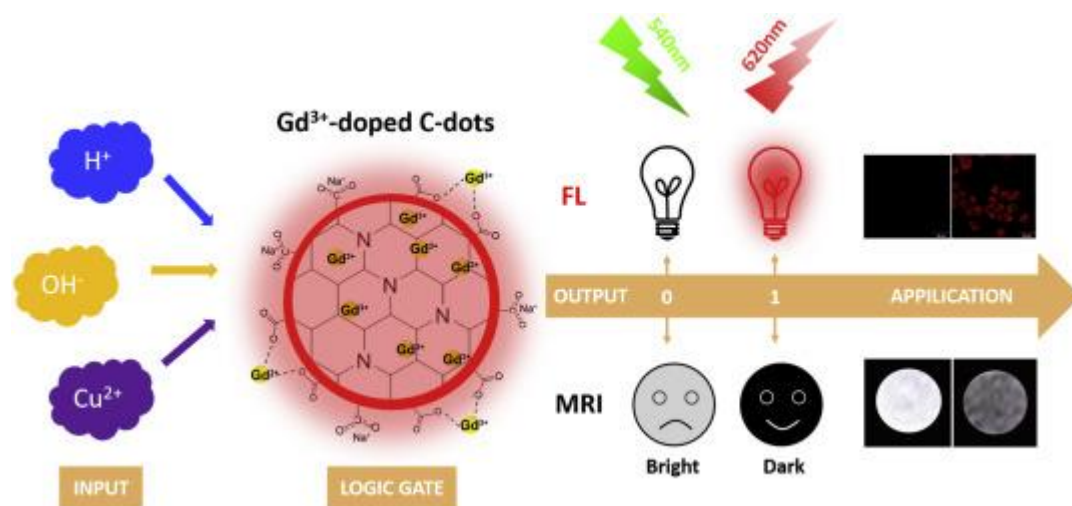


Fig. 1. Schematic diagram of the development and intracellular imaging application of FL/MR dual-readout logic operations based on the pH-responsive Gd³⁺-doped C-dots. (A colour version of this figure can be viewed online.)

2. Experimental

2.1. Reagents

3-(4,5-Dimethylthiazol-2-yl)-2,5-diphenyltetrazolium bromide (MTT), GdCl₃, xylenol orange and 4',6-diamidino-2-phenylindole (DAPI) were purchased from Sigma-Aldrich. Citric acid monohydrate (CA), urea, N,N-Dimethylformamide (DMF), Britton-Robinson buffer (BR buffer), phosphate buffered saline (PBS), and CuSO₄ were purchased from Sinopharm Chemical Reagent Co. Ltd. Reagents for cell culture including Dulbecco's Modified Eagle Medium with high glucose (H-DMEM), Fetal Bovine Serum (FBS), pancreatin and penicillin-streptomycin, were purchased from Gibco. All reagents mentioned above are of analytical grade and used without further purification.

2.2. Synthesis and characterization of the Gd^{3+} -doped C-dots

The Gd^{3+} -doped C-dots were synthesized *via* a solvothermal route. In brief, 1.0 g CA, 0.016 g $GdCl_3$ and 2.0 g urea were dissolved in 10.0 mL DMF and reacted in the autoclave at 160 °C for 6 h. After cooling down to room temperature, the obtained dark red solution was washed with 1.0 M NaOH aqueous solution under stirring for 5 min, followed by dialyzed (MWCO = 3500) against water for 3 days and centrifugation at 12,000 rpm for 10 min. Then, the precipitate was washed with de-ionized (D.I) water twice, and the as-prepared Gd^{3+} -doped C-dots were collected after being freeze-dried. Nanoparticles loaded on amorphous carbon-coated copper grids (Electron Microscopy China) were characterized by a JEM-2100F Transmission Electron Microscopy (TEM, JEOL) operated at 200 kV. Surface functional groups on the as-prepared nanoparticles were analyzed with an ESCALAB 250 X-ray photoelectron spectrometer (Thermo-VG Scientific) using mono-Al $K\alpha$ line (1486.71 eV) radiation. Powder X-ray diffraction (XRD) patterns were measured by a Rigaku SmartLab powder diffractometer (Rigaku) in the 2θ range of 10–80°, using Cu $K\alpha$ radiation source (40 kV, 30 mA). UV–Vis absorption spectra was recorded using a DU730 UV–vis spectrometer (Beckman). Zeta potential and dynamic light scattering (DLS) measurement were recorded on a NanoZS90 instrument (Malvern). All the fluorescence spectra were obtained with a Fluoromax-4P fluorescence spectrometer (Horiba) at room temperature. Fluorescence lifetime and fluorescence quantum yield were determined on a FSP920-combined time resolved and steady state fluorescence spectrometer (Edinburgh) and a quantum yield measurement system (Hamamatsu). MR properties was characterized on a clinical 1.5T MRI instrument (SIEMENS), where a standard inversion recovery pulse sequence was applied and water protons in D.I water was used as the blank.

2.3. General procedure for recording the FL and MR response of the Gd^{3+} -doped C-dots to H^+/OH^-

The Gd^{3+} -doped C-dots stock solution was prepared in D.I water. The fluorescence titration measurements were performed by adding 0.10 mL Gd^{3+} -doped C-dots (0.10 mg mL⁻¹) into 2.0 mL of BR buffer solution with pH value ranging from 1.0 to

10.0. Then, the mixtures were mixed well and kept 5 min before being subjected to a Horiba Fluoromax-4P fluorescence spectrometer for recording the FL response under excitation at 540 nm. Each experiment was performed in triplicate.

For recording the MR response of the Gd³⁺-doped C-dots to H⁺/OH⁻, 50 μL of 0.10 mg mL⁻¹ Gd³⁺-doped C-dots was added into the 1.0 mL of BR buffer solution with pH value ranging from 1.0 to 10.0. Then, the mixtures were mixed well and kept 5 min before being subjected to a 1.5 T human clinical scanner applied with a standard spinecho sequence. 500 ms TR (Time of Repeation) and 12 ms TE (Time of Echo) were used to collect T₁-Weighted MR images. Each experiment was performed in triplicate.

2.4. Biocompatibility of the Gd³⁺-doped C-dots

The leakage of the Gd³⁺ from the C-dots into serum was detected using xylenol orange as the indicator [46]. In brief, 3.0 mL of the Gd³⁺-doped C-dots solution (0.040 mg mL⁻¹) was subjected to dialysis against 27.0 mL PBS under centrifugation at 100 rpm. At different time points (0, 1, 2, 4, 8, 12, 24 h), 50 μL of sample was collected and mixed with 100 μL of xylenol orange (0.012 mg mL⁻¹) in a 96-well microplate. Then, the absorbance at 433 nm (Abs₄₃₃) and 573 nm (Abs₅₇₃) were measured.

MTT assay and the hemolysis assay were used to evaluate the cytotoxicity and blood compatibility of the Gd³⁺-doped C-dots, respectively. The experiment protocols are described in detail in Supporting Information [46]. In brief, HeLa cells at a density of 5 × 10³ cells per well were incubated for 24 h, followed by co-incubation with the Gd³⁺-doped C-dots (0, 0.05, 0.1, 0.2, 0.4, 0.6 mg mL⁻¹) for another 24 h. After the cells were washed by PBS for 3 times, 20 μL of MTT solution (dissolved in PBS, 5 mg mL⁻¹) were added to each well, and incubated for another 4 h. Finally, the absorbance at 570 nm was measured on a microplate reader. HeLa cells without the treatment of the Gd³⁺-doped C-dots were used as negative control group, and optical density (OD) of the negative control group represented 100% growth of the cells. The relative cytotoxicity was expressed as percentage of $[\text{OD}_{\text{sample}} - \text{OD}_{\text{blank}}]/[\text{OD}_{\text{control}} - \text{OD}_{\text{blank}}] \times 100$. For the hemolysis assay, 0.1 mL of red blood cells was mixed with

1.5 mL aqueous solution containing varying concentrations of the Gd³⁺-doped C-dots (0.05, 0.1, 0.2, 0.3, 0.4, 0.5, 0.6 mg mL⁻¹), and incubated for 2 h under mild shake. Then, the upper supernatants were collected for measuring the absorbance at 541 nm for the calculation of the hemolysis percentage using the following equation: Hemolysis (%) = (Abs_{sample} - Abs_{negative control}) / (Abs_{positive control} - Abs_{sample}) × 100%. 1.5 mL ultrapure water and PBS were used as positive and negative control, respectively.

2.5. General procedure for logic operations

For the IMP operation, the starting solutions containing 0.20 mg mL⁻¹ of the Gd³⁺-doped C-dots in PBS buffer (pH = 7.4) were first added to four tubes. Then, Input-1 (0.20 M HCl or 2.0 mM Cu²⁺) and Input-2 (0.20 M NaOH) were added according to their corresponding states for each logic operation (0,0; 0,1; 1,0; and 1,1). For NOR operation, the starting solutions containing 0.20 mg mL⁻¹ of the Gd³⁺-doped C-dots in PBS buffer (pH = 7.4) were first added to four tubes. Then, Input-1 (2.0 mM Cu²⁺) and Input-2 (0.20 M HCl) were added according to their corresponding states for each logic operation (0,0; 0,1; 1,0; and 1,1).

2.6. Dual-modal FL/MR cellular imaging

According to MTT results, the concentration of the Gd³⁺-doped C-dots solution for cellular imaging was 0.20 mg mL⁻¹ in H-DMEM. After incubated with the Gd³⁺-doped C-dots for 4 h, the HeLa cells were washed twice with PBS and fixed with 1 mL of 4% paraformaldehyde for 5 min, followed by washed with PBS and stained with 200 μL DAPI diluted twice for 10 min. The fluorescence images were acquired by a confocal laser scanning microscope (Leika, TCS-SP5) under UV excitation with a peak at ~359 nm and ~535 nm. For MR imaging, the HeLa cells were incubated with the Gd³⁺-doped C-dots for 4 h, followed by being washed twice with PBS. Then, the T₁-weighted MR images of the HeLa cells were acquired by a clinical 1.5T MRI instrument (Philip 1.5T Achieva), using the following scanning parameters: TR/TE = 480/8.8 ms, 256 × 196 matrices, and flip angle = 5°/26°.

3. Results and discussions

3.1. Characterization of the Gd^{3+} -doped C-dots

Typical TEM image of the Gd^{3+} -doped C-dots revealed that the as-prepared nanoparticles were well-separated and spherical in shape with a diameter of $\sim 2.0 \pm 1.0$ nm (Fig. 2A & B). The high-resolution TEM (HRTEM) images revealed an obvious lattice spacing of 0.205 nm and 0.334 nm, suggesting the (100) and (002) facet of graphene (Fig. 2C–E) [[51], [52], [53], [54]]. The crystal structure of the Gd^{3+} -doped C-dots was confirmed by the weak and broad diffraction peaks at $\sim 26.2^\circ$ in the XRD pattern of the Gd^{3+} -doped C-dots (Fig. 3A). The main diffraction peak at $\sim 26.2^\circ$ was ascribed to the (002) facet of graphite and indicated the high crystallinity of the Gd^{3+} -doped C-dots, since graphene with the ordered crystal structure exhibits a sharp diffraction peak at 26.5° in its XRD pattern [53,54]. The slightly shift of diffraction peaks (from 26.5° to 26.2°) indicated disordered carbon and decreased lattice spacing of sp^2 layers [54]. A typical amorphous carbonaceous structure of the Gd^{3+} -doped C-dots has also been revealed by the broad reflection in its XRD pattern. These results suggested that the Gd^{3+} -doped C-dots comprised a typical high crystalline graphene-based core and amorphous carbonaceous surface, resembling to most of previously reported C-dots [[46], [47], [48], [49], [50], [51], [52], [53], [54]].

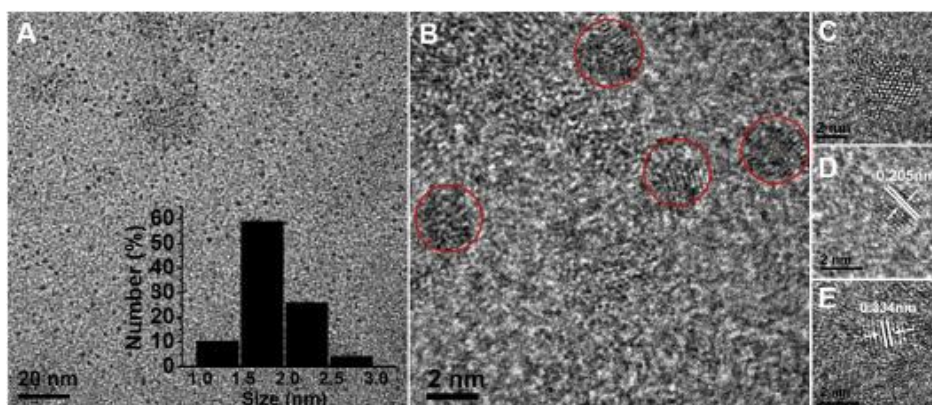


Fig. 2. Morphology. (A) TEM image of the Gd^{3+} -doped C-dots. Inset: the size distribution histogram of the Gd^{3+} -doped C-dots obtained from DLS

measurements; (B–E) High resolution TEM images of the Gd³⁺-doped C-dots showing the lattice spacing of 0.205 nm and 0.334 nm. (A colour version of this figure can be viewed online.)

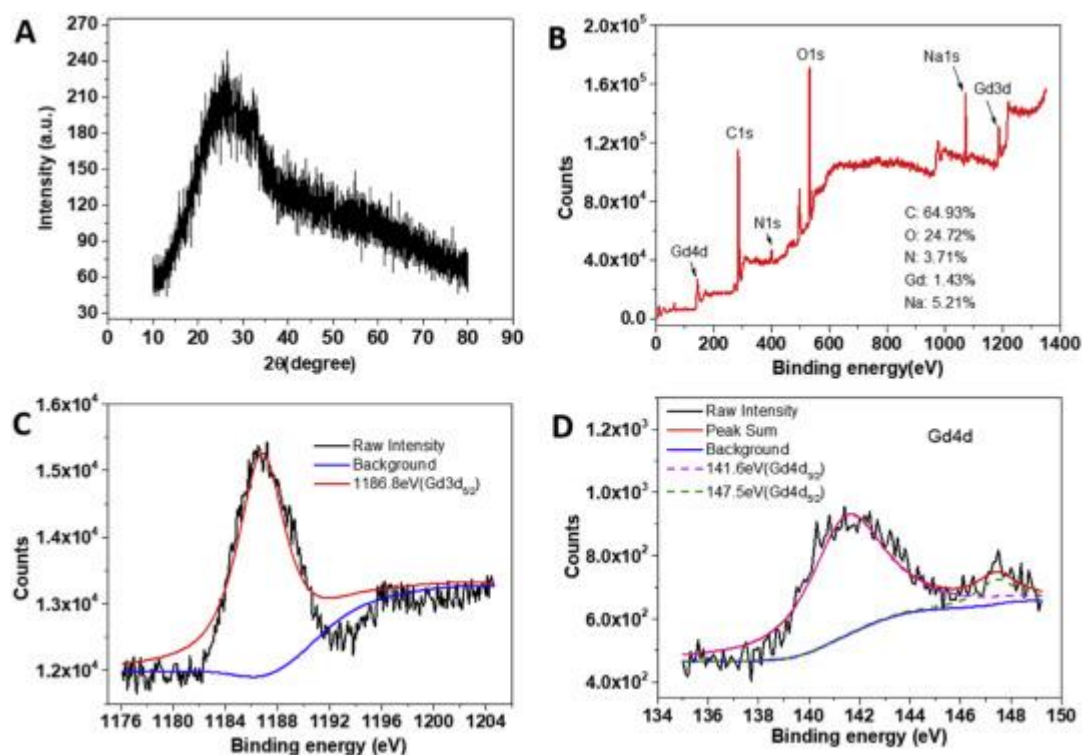


Fig. 3. Characterizations. (A) XRD patterns, (B) XPS survey spectra, and (C, D) the deconvoluted XPS spectra of the Gd³⁺-doped C-dots: (C) Gd 3d, (D) Gd 4d.

The successful doping of Gd³⁺ into C-dots is validated by its XPS survey spectra which exhibited the characteristic peaks corresponding to Gd 3d (1187 eV) and Gd 4d (142 eV) (Fig. 3B). Gd maintains its +3 oxidation state is quite important, because its half-filled *f* orbital with seven unpaired electrons and its symmetrical *s* ground state determine its MR imaging capability. However, it has been reported that magnetic and microwave properties of transition metal cations might be obviously changed due to the possibly increased charge state in the complex [55], [56], [57], [58]. It is reasonable that the electron density might shift from metal cations to more electronegative oxygen anions, leading to the altered electronic structure and thereby the magnetic and microwave properties [59,60]. Fortunately, the deconvoluted XPS Gd 4d spectra reveals the coexistence of Gd 4d_{5/2} (147.5 eV) and Gd 4d_{3/2} (141.6 eV) lines (Fig. 3C & D), verifying the +3 oxidation state of Gd after being doped into graphite matrix of

C-dots. Elemental analysis of XPS survey spectra revealed the presence of 1.43% Gd in the C-dots with 64.93% C, 24.72% O, 3.71% N, and 5.21% Na. In addition, inductively coupled plasma-mass spectrometry (ICP-MS) measurements confirmed the presence of total 32.6% (w/w) Gd content in the Gd³⁺-doped C-dots.

In addition, the XPS survey spectra also exhibited the characteristic peaks corresponding to C 1s (Fig S1A, 284.8 eV, 285.5 eV and 288.4 eV), N 1s (Fig S1B, 399.1 eV and 400.6 eV), O 1s (Fig S1C, 530.6 eV and 531.3 eV), and Na (Fig S1D, 1071.0 eV), revealing the main components of the Gd³⁺-doped C-dots were C, N, O, Gd, and Na. The presences of graphitic sp² carbon structure in the Gd³⁺-doped C-dots was also validated by the dominant peak centered at 284.8 eV in the deconvoluted XPS C 1s spectra which is attributed to C–C (Fig. S1A). Another two peaks presented in the deconvoluted XPS C 1s spectra should be attributed to C–O (288.4 eV) and C–N/C–O (285.5 eV), respectively. The successful doping of N elements was confirmed by the deconvoluted N 1s XPS spectra which exhibited a peak attributed to C–N (centered at 398.5 eV) (Fig. S1B), and the FTIR spectra which exhibited absorption peak of ν_{C-N} at 1396.2 cm⁻¹ (Fig. S1E). A dominant peak centered at 531.3 eV and a shoulder peak centered at 530.6 eV were found in the deconvoluted XPS O 1s spectra (Fig. S1C). These two peaks were respectively attributed to C–O and C–O, suggesting the presence of abundant surface carboxyl groups on the Gd³⁺-doped C-dots. This was also supported by the FTIR spectra which exhibited absorption peaks of ν_{O-H} (3407.7 cm⁻¹), $\nu_{C=O}$ (1575.6 cm⁻¹), ν_{C-O} (1112.7 cm⁻¹) (Fig. S1E). The abundant surface carboxyl groups which either inherited from the CA precursors and/or generated during the solvothermal process, can not only afford the resultant C-dots high water solubility, but also provide abundant chelating sites for Gd³⁺.

3.2. FL/MR Properties and biocompatibility of the Gd³⁺-doped C-dots

As shown in the Inset of Fig. 4A, the Gd³⁺-doped C-dots were highly water soluble, as evidenced by forming a homogeneous and dark red aqueous solution without visible precipitation for months. A shoulder peak at ~240 nm (attributed to $\pi \rightarrow \pi^*$ transition of

C) and an absorption peak centered at ~ 540 nm (attributed to large sized conjugated sp^2 -domain in the C-dots) [61] were observed in the UV-vis spectra of the Gd^{3+} -doped C-dots (curve a of Fig. 4A). These results further validated the graphitic sp^2 carbon structure in the Gd^{3+} -doped C-dots.

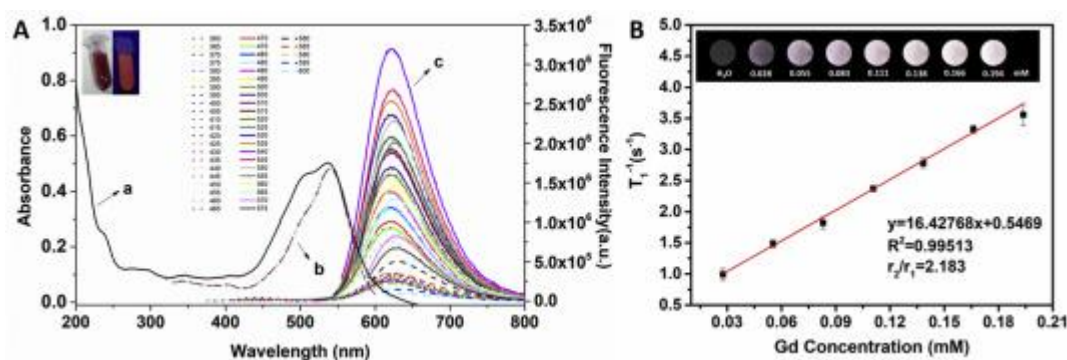


Fig. 4. Optical and MR properties of the Gd^{3+} -doped C-dots. (A) The UV-Vis absorption spectrum (curve a), FL excitation spectrum (curve b) and wavelength-independent FL emission spectra (curve c) of the Gd^{3+} -doped C-dots. The inset shows the photograph of the Gd^{3+} -doped C-dots under daylight and 365 nm UV light. (B) T_1 -weighted MR images of the Gd^{3+} -doped C-dots with various concentrations (equivalent Gd concentration: 0.028, 0.055, 0.083, 0.111, 0.138, 0.166, 0.194, mM), and linear correlation between T_1^{-1} and equivalent Gd concentration of the Gd^{3+} -doped C-dots. The longitudinal relaxivity (r_1) is the slope of the curve. (A colour version of this figure can be viewed online.)

By using fluorescent probes with red or near infrared (NIR) emission, low-background imaging could be realized for more accurate diagnosis through circumventing the scattering light of tissue and disturbance from auto-fluorescence. Therefore, red- or NIR-emissive C-dots are critically required for the practical biological applications, but still challenging [[62], [63], [64]]. Various protocols have been established to dope Gd^{3+} into C-dots with high efficiency, including hydrothermal treatment of CA, PEI, and Gd-DTPA [46], pyrolysis in air of Gd-DTPA [50], and solvothermal treatment of CA, ethanediamine, and $GdCl_3$ [51]. However, all those Gd^{3+} -doped C-dots emitted blue fluorescence. Recently, solvothermal treatment of p-phenylenediamine and

Gd(NO₃)₃ is reported to synthesize the Gd³⁺-doped C-dots which show a emission peak centered at ~580 nm under excitation at 550 nm [64].

In this study, a new solvothermal approach using CA, urea and GdCl₃ as precursors, is reported to prepare red-emissive Gd³⁺-doped C-dots. The as-prepared Gd³⁺-doped C-dots are highly fluorescent and exhibit a wavelength-independent emission, where the emission peak centered at ~620 nm under 360–600 nm excitation (curve c of Fig. 4A). The aqueous solution of the Gd³⁺-doped C-dots emitted bright red fluorescence centered at 620 nm under the max excitation wavelength of 540 nm (curve b of Fig. 4A) with a quantum yield (QY) of 2.3%. The fluorescence lifetime (τ) of the Gd³⁺-doped C-dots was determined to be 1.56 ns (Fig. S2A). In addition, the Gd³⁺-doped C-dots exhibited good photostability as evidence by no obvious photobleaching for up to 24 h under continuous UV irradiation (Fig. S2B). Bare C-dots without Gd³⁺ dopant can be synthesized *via* a similar solvothermal approach using CA and urea as precursors [61]. Compared with bare C-dots which exhibited a wavelength-independent emission peak centered at 580 nm (Fig. S3A), a red shift of *ca.* 40 nm in the emission wavelength and an obvious QY decrease, were observed after Gd³⁺ being doped into C-dots. The relation between the Gd dopant and FL emission properties of C-dots is still an open question, and in-depth investigations should be exquisitely designed for further elucidation. All these results confirm the good optical properties of the Gd³⁺-doped C-dots.

Gd³⁺ dopant enables the resultant Gd³⁺-doped C-dots MR imaging capability. As expected, the brightness of grey-scaled T₁-weighted MR images was obviously enhanced by the Gd³⁺-doped C-dots in a concentration-dependent manner (Inset of Fig. 4B). No positive contrast enhancement was observed for bare C-dots, also validating the successfully doping Gd³⁺ into C-dots (Fig. S3B). In addition, the r₁relaxivity of the Gd³⁺-doped C-dots was calculated to be 16.428 mM⁻¹s⁻¹ from the r₁relaxivity curve as fitted in Fig. 4B, suggesting Gd³⁺ after being doped into C-dot was still able to curtail the longitudinal relaxation time of hydrogen protons.

The Gd³⁺-doped C-dots exhibited good biocompatibility which guarantees their practical biological and biomedical applications. As shown in Fig. S4A, over 90% cell

viability was observed even when the cells were treated with the nanoparticles with concentrations up to 0.60 mg mL^{-1} . Besides the intrinsic biocompatibility of C-dots, the low cytotoxicity might also be ascribed to the negligible leakage of Gd^{3+} into serum for up to 72 h (Fig. S4B). In addition, the inset of Fig. S4C showed no visually red color, suggesting no swelling of red blood cells was caused by the Gd^{3+} -doped C-dots with concentrations up to 0.60 mg mL^{-1} . The highest hemolytic efficiency of the Gd^{3+} -doped C-dots was $\sim 3.0\%$ at its concentration up to 0.60 mg mL^{-1} (Fig. S4C), indicating the good blood compatibility.

3.3. pH-dependent FL emission and MR response of the Gd^{3+} -doped C-dots

Since pH plays a pivotal role in many biological events, pH sensing especially its intracellular imaging is of critical importance. pH sensing capacity of the Gd^{3+} -doped C-dots in aqueous solution was studied using BR buffer with pH values ranging from 1.0 to 10.0 under 540 nm excitation at room temperature (Fig. 5A and B). The Gd^{3+} -doped C-dots exhibit a pH-dependence only in the fluorescence intensity which increases as pH increases (Fig. 5A). Under alkaline conditions, the Gd^{3+} -doped C-dots emit strong red fluorescence, whereas, under extremely acidic conditions (pH 1.0), the fluorescence is nearly completely quenched (Fig. 5B). And if pH is switched repeatedly between 10.0 and 1.0, the FL emission intensity varies reversibly (Fig. S5A). The reversible protonation of surface carboxyl groups on the Gd^{3+} -doped C-dots might be responsible for the variation of the emission feature [[8], [9], [10], [11], [12],62].

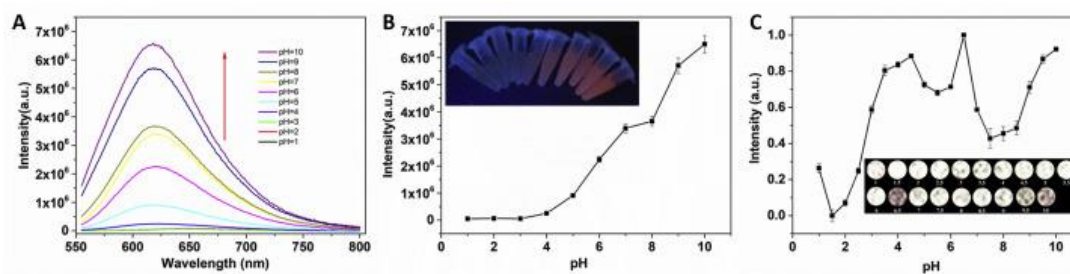


Fig. 5. pH-dependent FL emission and MR response of the Gd^{3+} -doped C-dots. (A) FL emission spectra of the Gd^{3+} -doped C-dots at different pH values. The arrow indicates the signal change with increasing pH (1.0, 2.0, 3.0, 4.0, 5.0, 6.0,

7.0, 8.0, 9.0, and 10.0). (B) A plot of the FL intensity at 620 nm (excitation at 540 nm) *versus* pH. The inset shows the photograph of the Gd³⁺-doped C-dots at different pH values under 365 nm UV light. (C) A plot of the MR intensity *versus* pH. The inset shows T₁-weighted MR images of the Gd³⁺-doped C-dots at different pH values. (A colour version of this figure can be viewed online.)

Interestingly, the Gd³⁺-doped C-dots also exhibit a pH-dependence in the MR response. Under extremely acidic conditions (pH 1.5), a significantly enhanced brightness of grey-scaled T₁-weighted MR image was obtained. When the pH increased to 4.0, MR response obviously decreased ([Fig. 5C](#)). Similarly, if pH is switched repeatedly between 10.0 and 1.0, the MR response varies reversibly ([Fig. S5A](#)). The reversible protonation of surface carboxyl groups on the Gd³⁺-doped C-dots might also be responsible for the variation of the MR response. It has been well-established that longitudinal relaxivity largely depends on direct interactions between Gd³⁺ and hydrogen protons [[65](#)]. In the Gd³⁺-doped C-dots, surface carboxyl groups can strongly coordinate with Gd³⁺, resulting in that the access of water molecules to the Gd³⁺ centre was restricted by steric hindrance and thus proton relaxivity was minimized. However, under extremely acidic conditions (pH 1.5), surface carboxyl groups will be protonated. And the protonation of carboxyl groups will restrict their coordination ability, thus relieving steric congestion around the Gd³⁺ centre and changing the relaxivity from weak to strong.

The alternations in cellular homeostasis of Cu²⁺ are connected various serious diseases such as Menkes and Wilson's diseases, Parkinson's and Alzheimer's diseases, and familial amyotrophic lateral sclerosis. It is herein of great importance to understand the relationships between Cu²⁺ regulation and its pathological consequences by monitoring and visualizing subcellular distribution of Cu²⁺. It has been well documented that carboxyl groups also exhibit strong coordination affinity towards Cu²⁺. Therefore, Cu²⁺ can bind to surface carboxyl groups of the Gd³⁺-doped C-dots, and thus quenching its fluorescence *via* inner filter effect mechanism [[66,67](#)]. And the competition between Cu²⁺ and Gd³⁺ for surface carboxyl groups on the Gd³⁺-doped C-dots, might also result

in relieving steric congestion around the Gd^{3+} centre and changing the relaxivity from weak to strong [68]. As expected, upon interaction with the Gd^{3+} -doped C-dots, Cu^{2+} also triggered both its FL turn-off and T_1 -weighted MR signal enhancement (Figs. S5B and 5C).

3.4. FL/MR dual-readout logic gates based on the Gd^{3+} -doped C-dots

A logic gate with multiple output signals may greatly improve its operation stability, however, only limited progress has been made in the development of multi-readout logic gates [34,42,[69], [70], [71]]. H^+ , OH^- and Cu^{2+} can trigger the FL and MR response switch of the Gd^{3+} -doped C-dots simultaneously, founding a solid base for the development of FL/MR dual-readout molecular logic gates. Therefore, in the Gd^{3+} -doped C-dots based logic operations, H^+ , OH^- and Cu^{2+} acted as chemical inputs, and their presence was defined as Boolean logic functions 1. The relative FL intensity at 620 nm of 0.5 and the relative MR intensity of 0.87 were set as the threshold value for the FL output and the MR output, respectively. Higher than the threshold value was defined as 1, whereas lower than the threshold value was defined as 0.

IMPLICATION (IMP) is a binary logic operation which produces the output of 0 only if the Input 1 is present and the Input 2 is absent. The Gd^{3+} -doped C-dots under neutral condition (input = 0,0) is fluorescent (FL output = 1), and exhibit no positive contrast enhancement (MR output = 1). OH^- alone (input = 0,1) can trigger both the FL enhancement (FL output = 1) and positive contrast attenuation (MR output = 1) of the Gd^{3+} -doped C-dots. And in the presence of both H^+ and OH^- (input = 1,1), the solution returns to neutral condition, thus exhibiting red fluorescence (FL output = 1) and no positive contrast enhancement (MR output = 1). However, the addition of H^+ only (input = 1,0) trigger both the fluorescence turn-off response (FL output = 0) and positive contrast enhancement (MR output = 0) of the Gd^{3+} -doped C-dots. These results correlate well with the proper execution of FL/MR dual-readout IMP logic operation (Fig. 6A). Since Cu^{2+} exhibit the same behaviour as H^+ towards the Gd^{3+} -doped C-dots, IMP logic operation can also be performed by employing Cu^{2+} as the Input 1 (Fig. 6B).

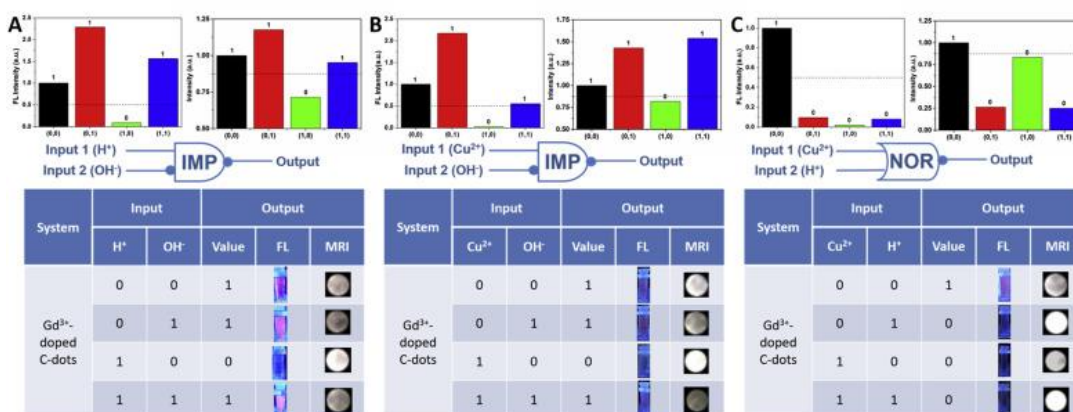


Fig. 6. FL/MR dual-readout logic gates based on the Gd³⁺-doped C-dots. (A) IMP logic operation using H⁺ as the Input 1 and OH⁻ as the Input 2. (B) IMP logic operation using Cu²⁺ as the Input 1 and OH⁻ as the Input 2. (C) NOR logic operation using Cu²⁺ and H⁺ as chemical inputs. From top to bottom: Normalized FL and MR intensity of the Gd³⁺-doped C-dots-based IMP gate with different input combinations; The symbol and the truth table of the IMP gate. (A colour version of this figure can be viewed online.)

In NOR logic operation, output 1 will be produced only in the absence of any inputs. Either Cu²⁺ (input = 1,0) or H⁺ (input = 0,1) can obviously trigger both the FL turn-off (FL output = 0) and T₁-weighted MR signal enhancement (MR output = 0) of the Gd³⁺-doped C-dots. The Gd³⁺-doped C-dots only exhibited strong red fluorescence (FL output = 1) and slight positive contrast enhancement (MR output = 1) in the absence of H⁺ and Cu²⁺ (input = 0,0). These results correlate well with the proper execution of FL/MR dual-readout NOR logic operation (Fig. 6C).

3.5. Living cell imaging based on IMP logic gate

In addition to develop sophisticate molecular devices using multiple inputs, how to condition logic systems for biomedical applications such as bioimaging and intelligent diagnostics have attracted more and more research attentions. Inspired by their good biocompatibility and the successful implementation of FL/MR dual-readout logic gates in all-aqueous media using the Gd³⁺-doped C-dots (Figs. S3 and 6), intracellular imaging with IMP logic operation has also been successfully demonstrated.

Different batches of HeLa cells pre-treated with the Gd^{3+} -doped C-dots for 4 h were incubated with standard culture medium and medium supplemented with Cu^{2+} , OH^- (buffer with pH value of 10.0) and ($Cu^{2+} + OH^-$) for another 30 min, respectively. The initial state (input = 0,0) was pH 7.4, therefore, clear cell morphology with red fluorescence only localized in cytoplasm (FL output = 1) and no obvious positive contrast enhancement (MR output = 1) were observed (Fig. 7A). When cells were incubated with Cu^{2+} ions alone (input = 1,0), the interaction between Cu^{2+} ions and the Gd^{3+} -doped C-dots resulted in the fluorescence quench (FL output = 0) and positive contrast enhancement (MR output = 0) (Fig. 7B). The addition of OH^- ions alone (input = 0,1) changed the pH value to 10.0, leading to the significantly enhanced FL signal (FL output = 1) and positive contrast attenuation (MR output = 1) (Fig. 7C). In the presence of both Cu^{2+} and OH^- (input = 1,1), the cells remain fluorescent (FL output = 1) and no obvious positive contrast enhancement (MR output = 1) were observed (Fig. 7D), because OH^- can interact with Cu^{2+} to diminish the interactions between Cu^{2+} and the Gd^{3+} -doped C-dots. These results correlate well with the proper execution of FL/MR dual-readout IMP logic operation, and demonstrate their successful implementation for intracellular imaging.

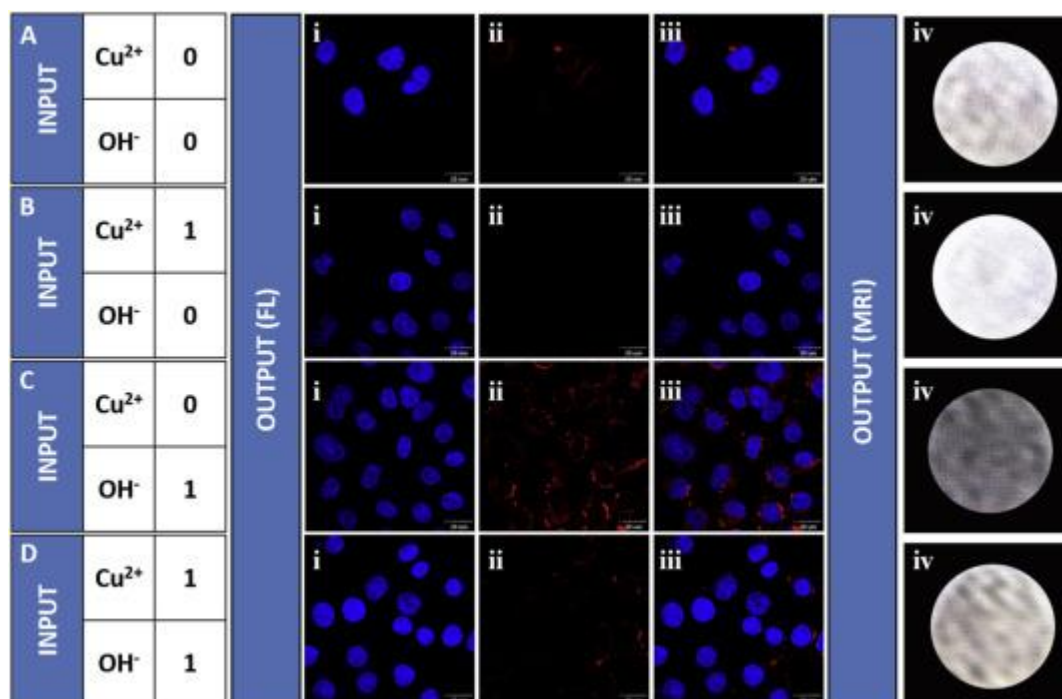


Fig. 7. Intercellular IMP logic operation was illustrated by both FL images and T₁-weighted MR images of the Gd³⁺-doped C-dots pre-treated HeLa cells after incubation in culture medium containing (A) blank (pH = 7.4); (B) Cu²⁺; (C) OH⁻ (pH = 10.0); (D) Cu²⁺ + OH⁻: (i) FL images at $\lambda_{\text{ex}}/\lambda_{\text{em}}$ of 359/461 nm; (ii) FL images at $\lambda_{\text{ex}}/\lambda_{\text{em}}$ of 535/617 nm; (iii) overlay of the FL images of the same cells; (iv) T₁-weighted MR images. (A colour version of this figure can be viewed online.)

4. Conclusion

In conclusion, the pH-responsive Gd³⁺-doped C-dots exhibiting strong red photoluminescence and high relaxivity has been synthesized using a facile one-step solvothermal approach, and successfully demonstrated for the development of FL/MR dual-readout logic systems. The distinctive advantage of this logic system is that molecular events could be monitored by both fluorescence spectroscopy, MRI scanner, and even the naked eye, which might significantly improve the stability of logic operations. And all the logic operations are performed in all-aqueous media, ensuring the entire environment-friendly operation and their biomedical applications. More importantly, the pH-responsive Gd³⁺-doped C-dots have been satisfactorily illustrated for the proper execution of FL/MR dual-readout IMP logic operation within biological cells, emphasizing their great potentials for future biological and biomedical applications with better applicability.

References

- [1] S.N. Baker, G.A. Baker *Angew. Chem. Int. Ed.*, 49 (2010), pp. 6726-6744
- [2] C.Q. Ding, A.W. Zhu, Y. Tian *Acc. Chem. Res.*, 47 (2014), pp. 20-30
- [3] K. Hola, Y. Zhang, Y. Wang, E.P. Giannelis, R. Zboril, A.L. Rogach *Nano Today*, 9 (2014), pp. 590-603
- [4] S.Y. Lim, W. Shen, Z.Q. Gao, *Chem. Soc. Rev.*, 44 (2015), pp. 362-381
- [5] Y. Du, S.J. Guo *Nanoscale*, 8 (2016), pp. 2532-2543

- [6] V. Sharma, P. Tiwari, S.M. Mobin *J. Mater. Chem. B*, 5 (2017), pp. 8904-8924
- [7] A. Abbas, L.T. Mariana, A.N. Phan *Carbon*, 140 (2018), pp. 77-99
- [8] A. Karimzadeh, M. Hasanzadeh, N. Shadjou, M. de la Guardia *Trac. Trends Anal. Chem.*, 108 (2018), pp. 110-121
- [9] A.A. Tregubov, P.I. Nikitin, M.P. Nikitin *Chem. Rev.*, 118 (2018), pp. 10294-10348
- [10] S. Erbas-Cakmak, S. Kolemen, A.C. Sedgwick, T. Gunnlaugsson, T.D. James, J. Yoon, E.U. Akkaya *Chem. Soc. Rev.*, 47 (2018), pp. 2228-2248
- [11] D. Bleger, S. Hecht *Angew. Chem. Int. Ed.*, 54 (2015), pp. 11338-11349
- [12] F. Wang, C.H. Lu, I. Willner *Chem. Rev.*, 114 (2014), pp. 2881-2941
- [13] F. Pu, J.S. Ren, X.G. Qu *Adv. Mater.*, 26 (2014), pp. 5742-5757
- [14] U. Pischel *Angew. Chem. Int. Ed.*, 46 (2007), pp. 4026-4040
- [15] A.P. de Silva, S. Uchiyama *Nat. Nanotechnol.*, 2 (2007), pp. 399-410
- [16] A.P. De Silva, H.Q.N. Gunaratne, C.P. McCoy *Nature*, 364 (1993), pp. 42-44
- [17] S. Erbas-Cakmak, O.A. Bozdemir, Y. Cakmak, E.U. Akkaya *Chem. Sci.*, 4 (2013), pp. 858-862
- [18] Y. Ling, Z.F. Gao, Q. Zhou, N.B. Li, H.Q. Luo *Anal. Chem.*, 87 (2015), pp. 1575-1581
- [19] D.L. Ma, H.Z. He, D.S.H. Chan, C.H. Leung *Chem. Sci.*, 4 (2013), pp. 3366-3380
- [20] D. Miyoshi, M. Inoue, N. Sugimoto *Angew. Chem. Int. Ed.*, 45 (2006), pp. 7716-7719
- [21] R.Z. Peng, X.F. Zheng, Y.F. Lyu, L.J. Xu, X.B. Zhang, G.L. Ke, Q.L. Liu, C.J. You, S.Y. Huan, W.H. Tan *J. Am. Chem. Soc.*, 140 (2018), pp. 9793-9796
- [22] J. Hemphill, A. Deiters *J. Am. Chem. Soc.*, 135 (2013), pp. 10512-10518
- [23] Y.L. Xianyu, Z. Wang, J.S. Sun, X.F. Wang, X.Y. Jiang *Small*, 10 (2014), pp. 4833-4838
- [24] Y. Zhang, Z.H. Shuai, H. Zhou, Z.M. Luo, B. Liu, Y.N. Zhang, L. Zhang, S.F. Chen, J. Chao, L.M. Weng, Q.L. Fan, C.H. Fan, W. Huang, L.H. Wang *J. Am. Chem. Soc.*, 140 (2018), pp. 3988-3993

- [25] Y.H. Lin, C. Xu, J.S. Ren, X.G. Qu, *Angew. Chem. Int. Ed.*, 51 (2012), pp. 12579-12583
- [26] Y. Pan, Y.P. Shi, Z.H. Chen, J.Y. Chen, M.F. Hou, Z.P. Chen, C.W. Li, C.Q. Yi *ACS Appl. Mater. Interfaces*, 8 (2016), pp. 9472-9482
- [27] Y. Pan, Y.P. Shi, J.Y. Chen, C.M. Wong, H. Zhang, M.J. Li, C.W. Li, C.Q. Yi *Materials Science & Engineering C-Materials*, 69 (2016), pp. 561-568
- [28] L.Y. Feng, Z.Z. Lyu, A. Offenhausser, D. Mayer *Angew. Chem. Int. Ed.*, 54 (2015), pp. 7693-7697
- [29] M.N. Stojanovic, T.E. Mitchell, D. Stefanovic *J. Am. Chem. Soc.*, 124 (2002), pp. 3555-3561
- [30] S. Muramatsu, K. Kinbara, H. Taguchi, N. Ishii, T. Aida *J. Am. Chem. Soc.*, 128 (2006), pp. 3764-3769
- [31] J.J. Zhang, Y. Lu *Angew. Chem. Int. Ed.*, 57 (2018), pp. 9702-9706
- [32] W.J. Wang, S. Huang, J.J. Li, K. Rui, S. Bi, J.R. Zhang, J.J. Zhu *Chem. Sci.*, 8 (2017), pp. 174-180
- [33] K.L. Zhao, Y. Tang, Z. Wang, J. Zhang, C.Y. Lei, H.H. Wang, H. Li, Y. Huang, Z. Nie, S.Z. Yao *Chem. Commun.*, 53 (2017), pp. 11326-11329
- [34] D.B. Liu, W.W. Chen, K. Sun, K. Deng, W. Zhang, Z. Wang, X.Y. Jiang *Angew. Chem. Int. Ed.*, 50 (2011), pp. 4103-4107
- [35] F. Pu, E.G. Ju, J.S. Ren, X.G. Qu *Adv. Mater.*, 26 (2014), pp. 1111-1117
- [36] A.P. De Silva, M.R. James, B.O.F. McKinney, D.A. Pears, S.M. Weir *Nat. Mater.*, 5 (2006), pp. 787-790
- [37] N. Dhenadhayalan, K.C. Lin *Sci. Rep.* (2015), p. 5
- [38] V. Sharma, N. Kaur, P. Tiwari, A.K. Saini, S.M. Mobin *Carbon*, 139 (2018), pp. 393-403
- [39] R.J. Gui, H. Jin, Z.H. Wang, F.F. Zhang, J.F. Xia, M. Yang, S. Bi, Y.Z. Xia *Nanoscale*, 7 (2015), pp. 8289-8293
- [40] X.J. Gong, Z.B. Li, Q. Hu, R.X. Zhou, S.M. Shuang, C. Dong *ACS Appl. Mater. Interfaces*, 9 (2017), pp. 38761-38772
- [41] W.S. Zou, Q.C. Zhao, W.L. Kong, X.F. Wang, X.M. Chen, J. Zhang, Y.Q. Wang

- Chem. Eng. J., 337 (2018), pp. 471-479
- [42] Y.F. Gao, Y. Jiao, W.J. Lu, Y. Liu, H. Han, X.J. Gong, M. Xian, S.M. Shuang, C. Dong, J. Mater. Chem. B, 6 (2018), pp. 6099-6107
- [43] W.J. Zhang, S.G. Liu, L. Han, H.Q. Luo, N.B. Li Sensor. Actuator. B Chem., 283 (2019), pp. 215-221
- [44] O.S. Yakovenko, L.Yu Matzui, L.L. Vovchenko, A.V. Trukhanov, I.S. Kazakevich, S.V. Trukhanov, Y.I. Prylutsky, U. Ritter, J. Mater. Sci., 52 (2017), pp. 5345-5358
- [45] O.S. Yakovenko, L.Yu Matzui, L.L. Vovchenko, O.V. Lozitsky, O.I. Prokopov, O.A. Lazarenko, A.V. Zhuravkov, V.V. Oliynyk, V.L. Launets, S.V. Trukhanov, A.V. Trukhanov, Mol. Cryst. Liq. Cryst., 661 (2018), pp. 68-80
- [46] Y. Pan, J. Yang, Y.N. Fang, J.H. Zheng, R. Song, C.Q. Yi J. Mater. Chem. B, 5 (2017), pp. 92-101
- [47] Y.N. Fang, J. Jia, J. Yang, J.H. Zheng, C.Q. Yi Chin. Chem. Lett., 29 (2018), pp. 1277-1280
- [48] Y.P. Shi, Y. Pan, J. Zhong, J. Yang, J.H. Zheng, J.L. Cheng, R. Song, C.Q. Yi Carbon, 93 (2015), pp. 742-750
- [49] D.L. Ni, W.B. Bu, S.J. Zhang, X.P. Zheng, M. Li, H.Y. Xing, Q.F. Xiao, Y.Y. Liu, Y.Q. Hua, L.P. Zhou, W.J. Peng, K.L. Zhao, J.L. Shi Adv. Funct. Mater., 24 (2014), pp. 6613-6620
- [50] H.M. Chen, G.D. Wang, W. Tang, T. Todd, Z.P. Zhen, C. Tsang, K. Hekmatyar, T. Cowger, R.B. Hubbard, W.Z. Zhang, J. Stickney, B.Z. Shen, J. Xie Adv. Mater., 26 (2014), pp. 6761-6766
- [51] Y. Xu, X.H. Jia, X.B. Yin, X.W. He, Y.K. Zhang Anal. Chem., 86 (2014), pp. 12122-12129
- [52] Y.Q. Dong, R.X. Wang, H. Li, J.W. Shao, Y.W. Chi, X.M. Lin, G.N. Chen Carbon, 50 (2012), pp. 2810-2815
- [53] M.M. Zhang, H.X. Ju, L. Zhang, M.Z. Sun, Z.W. Zhou, Z.Y. Dai, L.R. Zhang, A.H. Gong, C.Y. Wu, F.Y. Du, Int. J. Nanomed., 10 (2015), pp. 6943-6953
- [54] W.N. Yang, H. Zhang, J.X. Lai, X.Y. Peng, Y.P. Hu, W. Gu, L. Ye Carbon, 128 (2018), pp. 78-85

- [55] S.V. Trukhanov, L.S. Lobanovski, M.V. Bushinsky, V.V. Fedotova, I.O. Troyanchuk, A.V. Trukhanov, V.A. Ryzhov, H. Szymczak, R. Szymczak, M. Baran *J. Phys. Condens. Matter*, 17 (2005), pp. 6495-6506
- [56] S.V. Trukhanov, A.V. Trukhanov, C.E. Botez, A.H. Adair, H. Szymczak, R. Szymczak *J. Phys. Condens. Matter*, 19 (2007), p. 266214
- [57] M.A. Almessiere, A.V. Trukhanov, F.A. Khan, Y. Slimani, N. Tashkandi, V.A. Turchenko, T.I. Zubar, D.I. Tishkevich, S.V. Trukhanov, L.V. Panina, A. Baykal *Ceram. Int.*, 46 (2020), pp. 7346-7354
- [58] M.A. Almessiere, Y. Slimani, H. Güngüneş, V.G. Kostishyn, S.V. Trukhanov, A.V. Trukhanov, A. Baykal *Ceram. Int.*, 46 (2020), pp. 11124-11131
- [59] S.V. Trukhanov, I.O. Troyanchuk, M. Hervieu, H. Szymczak, K. Bärner *Phys. Rev. B*, 66 (2002), p. 184424
- [60] I.O. Troyanchuk, S.V. Trukhanov, G. Szymczak *Crystallogr. Rep.*, 47 (2002), pp. 658-665
- [61] S.N. Qu, D. Zhou, D. Li, W.Y. Ji, P.T. Jing, D. Han, L. Liu, H.B. Zeng, D.Z. Shen *Adv. Mater.*, 28 (2016), pp. 3516-3521
- [62] V. Strauss, J.T. Margraf, C. Dolle, B. Butz, T.J. Nacken, J. Walter, W. Bauer, W. Peukert, E. Spiecker, T. Clark, D.M. Guldi, *J. Am. Chem. Soc.*, 136 (2014), pp. 17308-17316
- [63] H. Ding, S.B. Yu, J.S. Wei, H.M. Xiong *ACS Nano*, 10 (2016), pp. 484-491
- [64] H.M. Chen, Y.W. Qiu, D.D. Ding, H.R. Lin, W.J. Sun, G.D. Wang, W.C. Huang, W.Z. Zhang, D.Y. Lee, G. Liu, J. Xie, X.Y. Chen *Adv. Mater.*, 30 (2018), p. 1802748
- [65] P. Caravan, J.J. Ellison, T.J. McMurry, R.B. Lauffer *Chem. Rev.*, 99 (1999), pp. 2293-2352
- [66] Y.Q. Dong, R.X. Wang, H. Li, J.W. Shao, Y.W. Chi, X.M. Lin, G.N. Chen *Carbon*, 50 (2012), pp. 2810-2815
- [67] Y. Dong, R. Wang, G. Li, C. Chen, Y. Chi, G. Chen *Anal. Chem.*, 84 (2012), pp. 6220-6224
- [68] X. Zhang, X. Jing, T. Liu, G. Han, H. Li, C. Duan *Inorg. Chem.*, 51 (2012), pp. 2325-2331

[69] A.K. Singh, P.K. Yadav, N. Kumari, R. Nagarajan, L. Mishra *J. Mater. Chem. C*, 3 (2015), pp. 12123-12129

[70] S.G. Liu, T. Liu, N. Li, S. Geng, J.L. Lei, N.B. Li, H.Q. Luo *J. Phys. Chem. C*, 121 (2017), pp. 6874-6883

[71] W.Y. Xie, W.T. Huang, N.B. Li, H.Q. Luo *Chem. Commun.*, 48 (2012), pp. 82-84